Nonlinear decay of high-power microwaves into trapped modes in inhomogeneous plasma

LETTER

Nonlinear decay of high-power microwaves into trapped modes in inhomogeneous plasma

IOP Publishing | International Atomic Energy Agency Nuclear Fusion

Nucl. Fusion **62** (2022) 074003 (6pp) https://doi.org/10.1088/1741-4326/ac5d61

Letter

Nonlinear decay of high-power microwaves into trapped modes in inhomogeneous plasma

A. Tancetti[1,*], S.K. Nielsen[1], J. Rasmussen[1], E.Z. Gusakov[2], A.Yu. Popov[2], D. Moseev[3], T. Stange[3], M.G. Senstius[1], C. Killer[3], M. Vecséi[4], T. Jensen[1], M. Zanini[3], I. Abramovic[5], M. Stejner[1], G. Anda[4], D. Dunai[4], S. Zoletnik[4], H.P. Laqua[3] and the W7-X Team[3,a]

[1] Department of Physics, Technical University of Denmark, Fysikvej, DK-2800 Kgs. Lyngby, Denmark
[2] Ioffe Institute, St. Petersburg, Russian Federation
[3] Max Planck Institute für Plasmaphysik, Greifswald, Germany
[4] Centre for Energy Research, Budapest, Hungary
[5] Eindhoven University of Technology, Eindhoven, Netherlands

E-mail: antan@fysik.dtu.dk

Received 18 January 2022, revised 24 February 2022
Accepted for publication 14 March 2022
Published 28 April 2022

Abstract

We present novel experimental evidence of parametric decay instability of microwave beams in the plasma edge of the Wendelstein 7-X stellarator. We propose that the instability is sustained by trapping of only one daughter wave in the non-monotonic density profile measured with high spatial resolution within a stationary magnetic island. The power levels and spectral shapes of the detected microwave signal are reproduced by numerical modelling and a theoretical power threshold is predicted around 300 kW, comparable with observations. We predict a fraction of power drained by daughter waves around 4% in the experiments, potentially increasing above 50% for more hollow edge density profiles. Such absorption levels could significantly reduce the efficiency of the microwave heating and current-drive system in tokamaks and stellarators.

Keywords: parametric decay instability, upper hybrid wave, ion Bernstein waves, electron cyclotron resonance heating, collective Thomson scattering, Wendelstein 7-X stellarator

(Some figures may appear in colour only in the online journal)

1. Introduction

When a high-power wave propagates in a plasma, nonlinear decay into a pair of daughter waves may occur, if the pump power exceeds a given threshold. The interaction is called parametric decay instability (PDI) and is ubiquitous in media with a second-order non-linearity, such as plasmas [1, 2], fluids [3, 4], and optical crystals [5]. In inhomogeneous media, if daughter waves are retained in a finite-size decay layer, an absolute PDI (APDI) can be excited, with temporal growth of the trapped waves' amplitude. In magnetized plasma, such a layer can be created by a non-monotonic density profile. This scenario is produced in ionospheric plasma by density depletion regions called striations [6]; APDI of upper hybrid waves (UHWs) propagating across the striation excites trapped UHWs and lower hybrid waves [7, 8].

* Author to whom any correspondence should be addressed.
[a] See Klinger et al 2019 (https://doi.org/10.1088/1741-4326/ab03a7) for the W7-X Team.

Similarly, in magnetically confined fusion plasmas, non-monotonic density profiles are generated by magnetic islands and edge localized modes. In these cases, anomalous microwave signals observed in TEXTOR [9] and ASDEX Upgrade [10] tokamaks during second-harmonic extraordinary (X2) electron cyclotron resonance heating (ECRH) were explained with APDI into a pair of trapped UHWs at half the pump frequency [11]. However, the wave trapping mechanism could not be assessed, since the decay region was poorly diagnosed.

In this letter, we present experimental evidence of PDI in the Wendelstein 7-X (W7-X) stellarator [12] where ECRH beams cross a stationary magnetic island in the plasma edge. High-quality measurements of the density bump in the island support the possibility of localization of the primary UHWs and ion Bernstein waves (IBWs). We present a theoretical model that reproduces the power and the spectrum of the PDI-related signal and predicts a theoretical power threshold around 300 kW, comparable to the experimental observations. For the experiments under consideration, the developed model predicts 4% of the injected microwave power to be converted into daughter waves, exceeding 50% for density bumps more prominent than those measured. Such strong pump power absorption, between 40 and 80%, was experimentally observed in the linear device granite [13]. This would significantly reduce the efficiency of the microwave injection system, fundamental for plasma heating and current drive in fusion plasmas, and hamper the operation of microwave diagnostics [14]. At the same time, supra-thermal ion or electron populations [15, 16] can be generated by parametrically driven UHWs and IBWs. On the one hand, these waves can potentially be exploited as an auxiliary plasma heating mechanism. On the other hand, such supra-thermal electron populations in the plasma edge might damage plasma-facing probes. A better understanding of PDI and of the conditions needed to excite or prevent it, could thus be used to increase the heating efficiency and fusion gain in such experiments.

2. Theoretical model

Consider the density profile in figure 1 where x is the direction along the inhomogeneity, perpendicular to the uniform background magnetic field, $\mathbf{B} = B\hat{z}$. An incoming pump beam with frequency ω_0^+ could decay into a trapped UHW, $\omega_1^+ < \omega_0/2$, and a back-scattered X-mode, ω_2^-, as shown in figure 2, where ' + ' and ' − ' refer to inward (decreasing x) and outward direction of propagation. Conservation of energy and momentum imply $\omega_0^+ = \omega_1^+ + \omega_2^-$, and $\mathbf{k}_0 = \mathbf{q}_{Em} + \mathbf{k}_\mathrm{p}$ where $\mathbf{k}_0$, $\mathbf{q}_{Em}$, and $\mathbf{k}_\mathrm{p}$ are wave-vectors of the pump, the trapped UHW, and back-scattered X-mode, while m is the eigenvalue of the resonant UHW.

For the pump X-mode wave, the cold dispersion relation reads

$$k_0 = \frac{\omega_0}{c}\sqrt{1 - \frac{\omega_\mathrm{pe}^2}{\omega_0^2}\frac{\omega_0^2 - \omega_\mathrm{pe}^2}{\omega_0^2 - \omega_\mathrm{UH}^2}}, \tag{1}$$

where $k_0 = |\mathbf{k}_0|$, c is the speed of light in vacuum, $\omega_\mathrm{UH} = (\omega_\mathrm{ce}^2 + \omega_\mathrm{pe}^2)^{1/2}$ is the upper hybrid frequency, $\omega_\mathrm{ce} = qB/m_\mathrm{e}$ and

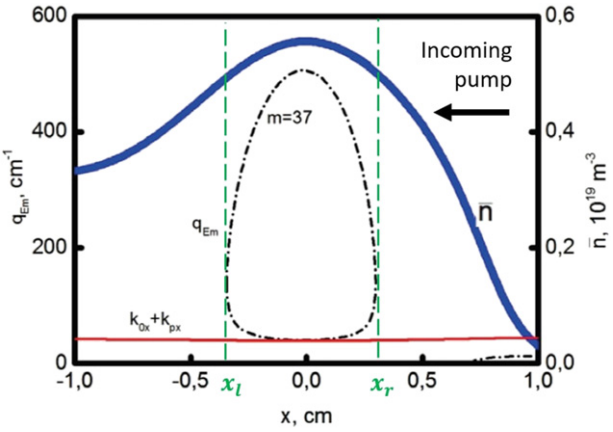

Figure 1. Density profile (blue) used to study PDI in the edge island of W7-X and 1D dispersion curves for the primary trapped UHW, q_{Em} (dashed-dotted loop), and scattered X-mode up-shifted by the pump wavenumber, $k_0 + k_\mathrm{p}$ (red). The point $x = 0$ cm corresponds to the maximum of the density profile.

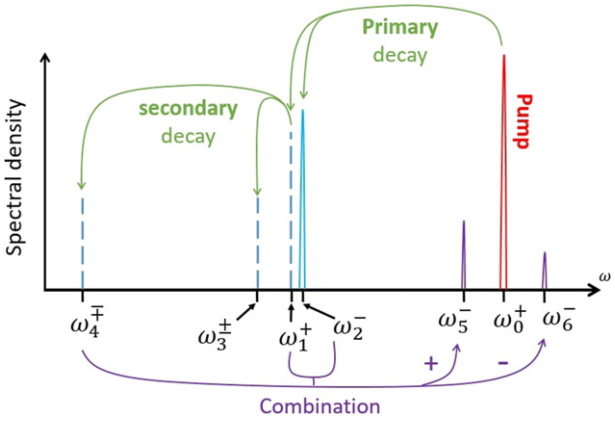

Figure 2. PDI cascade proposed in the theoretical model for X2-ECRH in W7-X. Dashed lines indicate waves trapped in the density bump.

$\omega_\mathrm{pe} = (n_\mathrm{e}q^2/(\varepsilon_0 m_\mathrm{e}))^{1/2}$ are the electron cyclotron and plasma frequency, ε_0 is the vacuum permittivity, and n_e, m_e, q, are the electron density, mass, and electric charge, respectively. The same dispersion relation applies to the escaping X-mode daughter with (k_p, ω_2). For the trapped UHW, the dispersion relation is

$$q_{Em}^{\pm} = \frac{1}{l_\mathrm{T}}\sqrt{-\frac{S}{2} \mp \frac{S}{2}\sqrt{1 + \frac{4\omega_1^2}{c^2}\frac{(S^2 - D^2)}{S^2}l_\mathrm{T}^2}}, \tag{2}$$

where $q_{Em}^{\pm}$ are the warm (+) and cold (−) branches of the UH dispersion curve, $l_\mathrm{T}^2 = 3\omega_\mathrm{pe}^2\omega_\mathrm{ce}^2 r_\mathrm{Le}^2/([4\omega_\mathrm{ce}^2 - \omega_1^2][\omega_1^2 - \omega_\mathrm{ce}^2])$, with $r_\mathrm{Le} = v_\mathrm{Te}/(\sqrt{2}|\omega_\mathrm{ce}|)$ and $v_\mathrm{Te} = (2T_\mathrm{e}/m_\mathrm{e})^{1/2}$ the electron Larmor radius and thermal velocity. The quantities $S = 1 - \omega_\mathrm{pe}^2/(\omega_1^2 - \omega_\mathrm{ce}^2)$ and $D = \omega_\mathrm{ce}\omega_\mathrm{pe}^2/(\omega_1(\omega_1^2 - \omega_\mathrm{ce}^2))$ are the sum and difference components of the cold plasma dielectric tensor [17] for the trapped mode. The value of m is found from the Bohr–Sommerfeld quantization condition:

$$\int_{x_l}^{x_r} |q_{Em}^+| - |q_{Em}^-|\,\mathrm{d}x = (2m+1)\pi, \tag{3}$$

with x_l and x_r coordinates of the inversion points, where $\omega_{\mathrm{UH}}(x_r) = \omega_{\mathrm{UH}}(x_l) = \omega_1$.

In figure 1, resulting dispersion curves are plotted for electron temperature $T_\mathrm{e} = 40$ eV, ion temperature $T_\mathrm{i} = 30$ eV, and $B = 2.23$ T, values measured in the plasma edge in our experiments. The loop displayed by $\mathbf{q}_{Em}$ confirms confinement of the mode around the density maximum. Build-up of primary UHWs in the cavity is saturated by the secondary decay into an UHW, $\omega_3^{\pm}$, and an IBW, $f_4^{\mp} = \omega_4^{\mp}/(2\pi) = 0.93$ GHz propagating in opposite directions (see figure 2). Trapping of the secondary daughter waves within the density bump increases the strength of the nonlinear coupling, compared to mechanisms involving escaping waves [18].

Finally, higher order plasma non-linearities leading to four-wave interactions, and particularly the combination of the scattered X-mode with the primary UHW and with IBWs, may excite high frequency modes at ω_5^- and ω_6^-, as shown in figure 2,

$$\omega_2^- + \omega_1^+ + \omega_4^{+,-} = \omega_{5,6}^-, \tag{4}$$

where the order of the subscripts on the right-hand side corresponds to the order of the superscripts on ω_4.

A more comprehensive description of the process must include diffraction losses along the poloidal direction, $\hat{y}$, and along the magnetic field lines, $\hat{z}$ ($\Lambda_{jy,z}$ with $j = 1, 3, 4$), and wave damping due to electron–ion collisions ($\nu_{1,3,4}$). If a_1, a_3, and b_4 are quantities proportional to the amplitude of the primary UHW, the secondary UHW, and the IBW respectively, the PDI-cascade is described by the following set of equations [19]:

$$\begin{cases} \dfrac{\partial a_1}{\partial t} - \mathrm{i}\Lambda_{1y}\dfrac{\partial^2 a_1}{\partial y^2} - \mathrm{i}\Lambda_{1z}\dfrac{\partial^2 a_1}{\partial z^2} = \\ \gamma_\mathrm{p}\exp\left(-\dfrac{y^2+z^2}{w^2}\right)a_1 - \gamma_\mathrm{s}^{+*}a_3^+ b_4^- - \gamma_\mathrm{s}^{-*}a_3^- b_4^+ - \nu_1 a_1 \\ \dfrac{\partial a_3^+}{\partial t} - \mathrm{i}\Lambda_{3y}\dfrac{\partial^2 a_3^+}{\partial y^2} - \mathrm{i}\Lambda_{3z}\dfrac{\partial^2 a_3^+}{\partial z^2} = \gamma_\mathrm{s}^+ a_1 b_4^{-*} - \nu_3 a_3^+ \\ \dfrac{\partial b_4^-}{\partial t} - \mathrm{i}\Lambda_{4y}\dfrac{\partial^2 b_4^-}{\partial y^2} - \mathrm{i}\Lambda_{4z}\dfrac{\partial^2 b_4^-}{\partial z^2} = \gamma_\mathrm{s}^+ a_1 a_3^{+*} - \nu_4 b_4^- \\ \dfrac{\partial a_3^-}{\partial t} + \mathrm{i}\Lambda_{3y}\dfrac{\partial^2 a_3^-}{\partial y^2} + \mathrm{i}\Lambda_{3z}\dfrac{\partial^2 a_3^-}{\partial z^2} = \gamma_\mathrm{s}^- a_1 b_4^{+*} - \nu_3 a_3^- \\ \dfrac{\partial b_4^+}{\partial t} + \mathrm{i}\Lambda_{4y}\dfrac{\partial^2 b_4^+}{\partial y^2} + \mathrm{i}\Lambda_{4z}\dfrac{\partial^2 b_4^+}{\partial z^2} = \gamma_\mathrm{s}^- a_1 a_3^{-*} - \nu_4 b_4^+ \end{cases} \tag{5}$$

where w is the width of the pump beam, $\gamma_{\mathrm{p,s}}$ are the nonlinear coupling coefficients for the primary (subscript 'p') and secondary ('s') decays, while asterisks denote complex conjugation.

A solution of equation (5) is computed in a 2D box with dimensions along $\hat{y}$ and $\hat{z}$ equal to $2y_B \times 2z_B$ much larger than the size of the pump using periodic boundary conditions following [19]. The time evolution of the daughter energy normalized to the thermal noise level, $\varepsilon_{1,3}(t) \propto |a_{1,3}(t)/a_{1,3}^{\mathrm{th}}|^2$ and $\varepsilon_4(t) \propto |b_4(t)/b_4^{\mathrm{th}}|^2$, is shown in figure 3, where $\langle \ldots \rangle$ denotes averaging across the pump beam cross section. The black line displays the exponential growth of the primary UHWs after pump injection ($t = 0$ s), with saturation around $t = 15$ μs. Dashed and dashed-dotted lines depict the evolution of

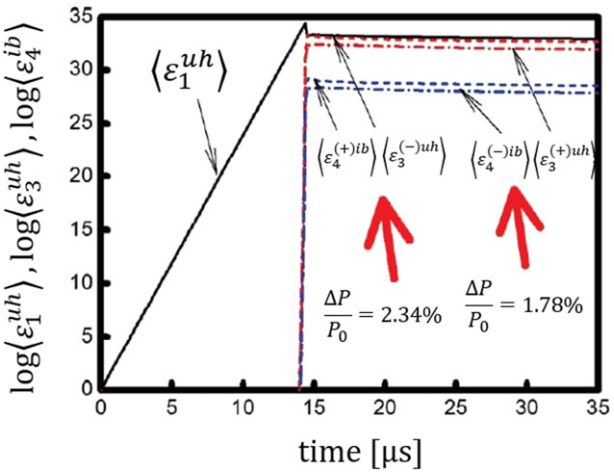

Figure 3. Energy of primary (black) and secondary (blue and red) trapped daughter waves. The fraction of drained power is given for both secondary mechanisms.

secondary daughter waves for the case with inward and outward propagating IBWs, respectively. The predicted fraction of pump power absorbed by the daughter waves sums up to 4%.

In order to compute the power threshold, P_0, for the primary instability, we put the instability growth rate $\gamma = 0$ [20]:

$$\gamma = |\gamma_\mathrm{p}| - \nu_\mathrm{ei}(T_\mathrm{e}) - \sqrt{\frac{|\gamma_\mathrm{p}|}{2w^2}}\left[(2l_z+1)\sqrt{\Lambda_{1z}} + (2l_y+1)\sqrt{\Lambda_{1y}}\right] = 0, \tag{6}$$

where l_y, l_z are the thickness of the interaction region along $\hat{y}$ and $\hat{z}$. In the low-temperature regime considered here, collisional energy losses dominate over diffraction, $\nu_\mathrm{ei}(T_\mathrm{e}) \gg \Lambda_{1y,z}/w^2$, hence equation (6) can be cast as $\gamma \approx |\gamma_\mathrm{p}| - \nu_\mathrm{ei}(T_\mathrm{e}) = 0$ where $|\gamma_\mathrm{p}| \propto P_0$. For $T_\mathrm{e} = 40$ eV, the condition yields $P_0 \approx 300$ kW.

Finally, we focus on the prediction of the spectral power density (SPD) for the peak at ω_5. The amplitude of the signal collected by the receiver antenna can be expressed in terms of the spatial distribution of the third-order non-linear current density, $\mathbf{j}_\mathrm{NL}(\omega_5, \mathbf{r})$, produced by the combination of waves at ω_1, ω_2, and ω_4^+ [20]:

$$A(\omega_5) = \frac{1}{4}\int \mathbf{j}_\mathrm{NL}(\omega_5, \mathbf{r})\mathbf{E}(\omega_5, \mathbf{r})\mathrm{d}\mathbf{r}, \tag{7}$$

where the integration is carried out over the whole plasma volume. Here, $\mathbf{E}(\omega_5, \mathbf{r})$ is the electric field of the beam on the receiver antenna operating as an emitting one at the opposite sign of the magnetic field and normalized to unit power. The power of the back-scattered signal can be computed as $p_\mathrm{s} = |A(\omega)|^2$. Assuming a spectrum line width, $\Delta\nu = 0.1$ GHz, for the peak at ω_5, the predicted SPD is given by $p_\mathrm{s}/\Delta\nu = 2.1$ MeV.

However, the intensity of the peaks at ω_5 and ω_6 does not only depend on the amplitude of the daughter waves, which affects the power absorption. It also depends on the strength of the nonlinear coupling between combining waves and so

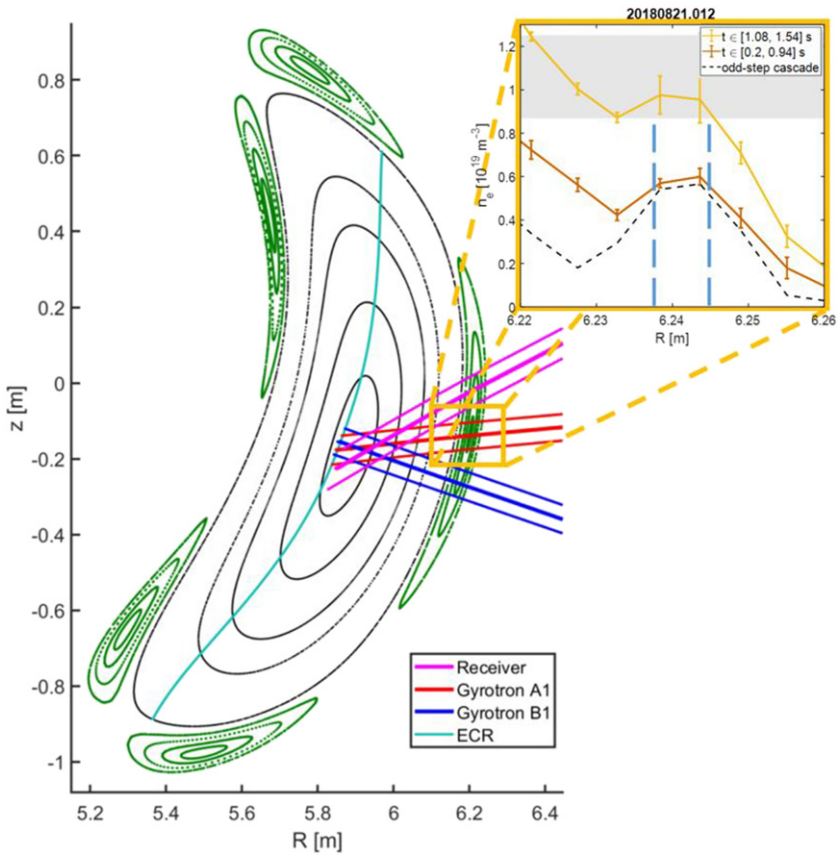

Figure 4. Poincaré plot of the standard magnetic configuration with green magnetic islands, microwave (gyrotron) beams (red and blue), and receiver line-of-sight (magenta). The top right inset displays alkali beam emission spectroscopy (ABES) density profiles (yellow and brown) and the profile predicted for a PDI cascade with an even number of secondary decays (dashed). Vertical dashed lines (light blue) outline the inversion points, i.e. the boundaries of the trapping region (see green vertical lines in figure 1), for daughter waves with $\omega_1/(2\pi) \approx 66$ GHz, for the brown density profile.

does not necessarily mirror the fraction of power absorbed by each channel. Since a stronger nonlinear combination is found for ω_4^+, the up-shifted sideband is expected to be weaker.

3. Experimental setup

The experimental observations were collected in W7-X during campaign OP1.2(a, b). In W7-X, superconducting coils produce the nested magnetic flux surfaces and the chain of five magnetic islands outside the last closed flux surface [21], shown in figure 4.

Plasma heating was accomplished via X2 ECRH with two 1 MW gyrotrons at $f_0 = 140$ GHz and on-axis magnetic field strength $B_0 = 2.52$ T. As shown in figure 4, the microwave beams are injected from the ECRH antennas on the right, intercept the equatorial-plane magnetic island, and are absorbed at the electron cyclotron resonance, shown in cyan.

The radiated microwave power is monitored with a highly sensitive radiometer with steerable line-of-sight, originally developed for collective Thomson scattering [22]. Gyrotron lines are blocked by notch filters and the signal is mixed down in two stages, and sampled using a PXIe-5186 digitizer, with sampling frequency $f_s = 6.25$ GS/s. The SPD of the signal is computed from its Fourier transform, with time and frequency resolution $\delta t = 0.6$ μs and $\delta f = 1.53$ MHz. A calibration is performed using blackbody sources at different temperatures [23].

4. Experimental results

Figure 5 shows results from discharge 20180821.12. Before $t = 1$ s (start-up phase), the hydrogen plasma is sustained by gyrotrons A1, with $P_{\mathrm{A1}} \sim 750$ kW, and B1, modulated between $P_{\mathrm{B1}} \sim 250$ and 500 kW, while the line-integrated density [24] grows up to $n_{\mathrm{e,LA}} = 3 \times 10^{19}$ m^{-2} (see figure 5(*a*)). Probe measurements [25] of $T_{\mathrm{e}} = 40$ eV and $T_{\mathrm{i}} = 30$ eV at the plasma edge correspond to the values used in the model above, with $B = 2.23$ T at the centre of the island. At $t = 1$ s, P_{A1} drops to 500 kW, whereas six more gyrotrons are turned on for a total ECRH power of $P_{\mathrm{tot}} = 4$ MW, inducing a steep rise of $n_{\mathrm{e,LA}}$.

Radial density profiles across the magnetic island measured by the ABES [26] are shown in the figure 4 inset. The mean density during the start-up phase is shown by the lower solid curve, while the tallest profile shows the mean between $t =$ 1.08–1.54 s. The grey-shaded area identifies the evanescent region for the primary extraordinary daughter wave, where PDI is inhibited.

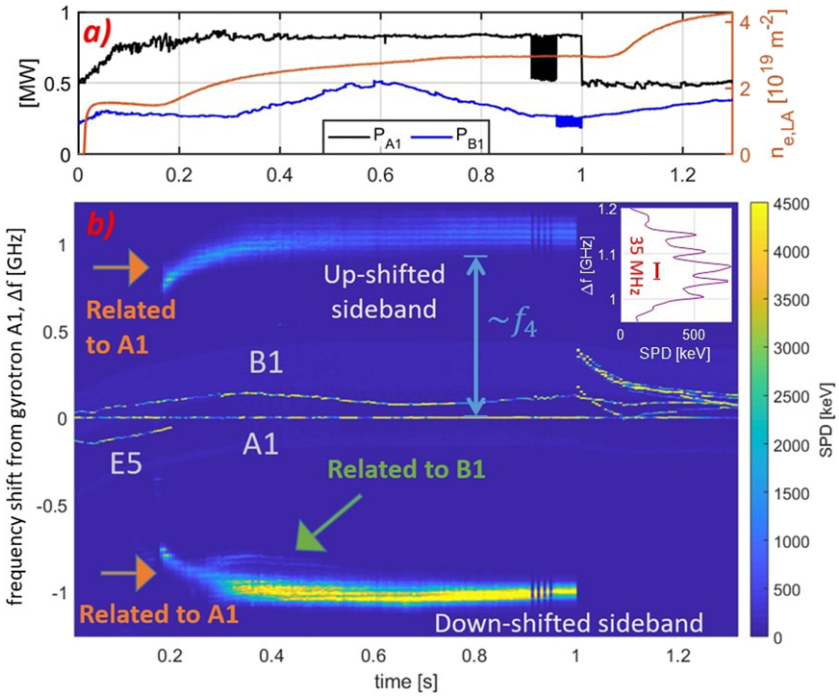

Figure 5. (*a*) Time-traces of $n_{e,LA}$, and ECRH power, P_{A1} and P_{B1}, for $t \leqslant 1.3$ s in discharge 20180821.012. (*b*) Corresponding calibrated mean spectrogram of the signal detected by the radiometer. Top right panel shows the mean SPD in the up-shifted sideband at $t = 0.72$ s.

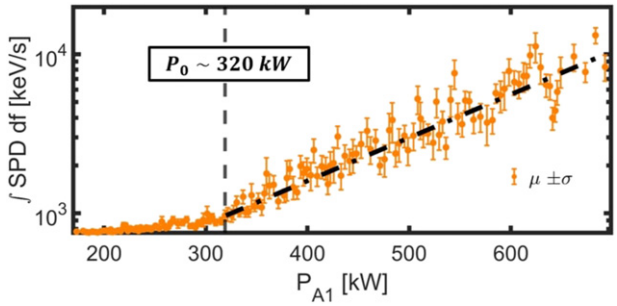

Figure 6. Intensity of the PDI-related down-shifted signal during modulation of P_{A1}. Orange points represent the mean of the signal, computed in different time-bins during the power ramp. The vertical line marks the experimental power threshold, $P_{0,XP} \approx 320$ kW.

The spectra detected by the radiometer are shown in figure 5(*b*), with frequency shift from gyrotron A1, Δf, on the y-axis. Thin lines around $\Delta f = 0$ GHz are produced by the gyrotron stray radiation. Two symmetric sidebands appear above the electron cyclotron emission background from $t \approx 0.18$ s and persist during the start-up phase. The frequency shift of the sidebands is comparable and grows from $|\Delta f| = 0.75$ to 1 GHz, and the band width, $\Delta\nu_{XP} \approx 0.1$ GHz, is in both cases similar to the value assumed in the theoretical section. Conversely, the power distribution is asymmetric, with 5–7 MeV in the down-shifted signal, and ∼1 MeV in the up-shifted counterpart. We note that the main signal in figure 5(*b*) responds to the frequency and power of gyrotron A1. The fine structure of each sideband, shown in the top right corner of figure 5(*b*), reveals thin spectral lines separated by ≈35 MHz.

In order to assess an experimental power threshold, a power ramp from $P_{A1} = 650$ to 150 kW was performed in a different discharge with $n_{e,LA} \sim 2.23 \times 10^{19}$ m^{-2}, an inward shifted magnetic configuration and plasma composition 50/50% H/He. The resulting intensity of the down-shifted sideband is plotted versus P_{A1} in figure 6. Orange points refer to the mean value (μ) and standard deviation (σ) of the signal in each power bin, respectively. Above $P_{A1} \approx 320$ kW the signal mean value grows exponentially.

5. Discussion

The model in equations (1)–(7) can reproduce consistently the measured spectra and the power of the PDI-related sidebands. The experimental frequency shift of the main bands, between $\Delta f = 0.75$–1 GHz, is comparable with the predicted frequency of the trapped IBWs, $f_4 = 0.93$ GHz. Experimental evidence of IBWs is provided by the spectral lines within each sideband, separated by the edge ion cyclotron frequency, $f_{IC}^{edge} \approx 35$ MHz. Furthermore, the dominant fraction of power is experimentally observed in the down-shifted component, in agreement with the evolution predicted in figure 3, and is consistent with the predicted SPD, $p_s/\Delta\nu$. The experimental power threshold, $P_{0,XP} \approx 320$ kW, is furthermore in good agreement with the theoretical value of $P_0 \approx 300$ kW for $T_e = 40$ eV. Exponential growth of the instability was observed above the threshold, confirming the nonlinear power scaling of the process involved.

PDI-related sidebands are excited only in the start-up phase, when the edge density profile lies below the evanescent region.

This suggests inhibition of PDI when the primary X-mode daughters cannot propagate. However, a density peak above the evanescent region would trigger the two-plasmon decay instability where both daughter waves, at half pump frequency, are retained in the cavity. Here, the quicker growth of the trapped UHWs could substantially lower the instability power threshold.

It is also crucial to monitor the shape of the edge density profile in order to prevent a significant increase of pump power absorption by the daughter waves. Density profiles similar to the dashed curve in figure 4 would allow trapping of tertiary UHWs with frequency $\omega_7 = \omega_3 - \omega_4$ within the density bump and consequently reduce the power threshold for the decay of secondary UHWs (ω_3) into a tertiary UHW and an IBW (ω_4). In a similar scenario, where build-up of secondary UHWs is saturated, pump depletion seems to become the principal saturation mechanism for the primary process. As found by modifying equation (5) to include a tertiary decay, following [19], the fraction of pump power absorbed by the daughter waves in similar circumstances results above 50%. Edge profiles displaying a more hollow density bump could, thus, have a major impact in the overall plasma discharge.

6. Conclusions

We have shown experimental evidence of PDI during X2 ECRH in W7-X and presented a model for PDI in the density bump measured with high-spatial resolution within the equatorial-plane magnetic island in the plasma edge. The density profile allows for trapping of a single primary and secondary UHWs and IBWs. The model reproduces the power and spectrum of the measured PDI signal, along with the observed power threshold $P_0 \approx 300$ kW. We predict the fraction of power absorbed by the daughter waves in the cascade, $\approx$4%, and predict scenarios where power absorption >50% could occur due to the onset of a tertiary instability. This would dramatically reduce the heating and current-drive efficiency of the microwave injection system in W7-X and in reactor-like environments like the ITER tokamak [27], additionally posing a serious hazard to the optimal operation of microwave-based diagnostics [14].

Acknowledgments

This work has been supported by research Grant 15483 from VILLUM FONDEN and the Enabling Research Grant ENR-MFE19.DTU-03 from the EUROfusion Consortium. The work has been carried out within the framework of the EUROfusion Consortium and has received funding from the Euratom research and training programme 2014–2018 and 2019–2020 under Grant No. 633053. The views and opinions expressed herein do not necessarily reflect those of the European Commission. The analytical theoretical treatment is supported under the Ioffe Institute state contract 0040-2019-0023, whereas the numerical modeling is supported under the Ioffe Institute state contract 0034-2021-0003.

ORCID iDs

A. Tancetti https://orcid.org/0000-0002-8048-007X
S.K. Nielsen https://orcid.org/0000-0003-4175-3829
J. Rasmussen https://orcid.org/0000-0002-3947-1518
A.Yu. Popov https://orcid.org/0000-0003-0574-516X
M.G. Senstius https://orcid.org/0000-0001-9596-7457
C. Killer https://orcid.org/0000-0001-7747-3066
M. Vecséi https://orcid.org/0000-0003-4596-1211
M. Zanini https://orcid.org/0000-0002-8717-1106
S. Zoletnik https://orcid.org/0000-0002-7324-2647

References

[1] McDermott F.S. *et al* 1982 *Phys. Fluids* **25** 1488–90
[2] Wilhelm R., Erckmann V., Janzen G., Kasparek W., Muller G., Rauchle E., Schuller P.G., Schworer K. and Thumm M. 1984 *Plasma Phys. Control. Fusion* **26** 1433
[3] Michel G. 2019 *Phys. Rev. Fluids* **4** 012801
[4] Haudin F. *et al* 2016 *Phys. Rev.* E **93** 043110
[5] Guo X. *et al* 2016 *Phys. Rev. Lett.* **117** 123902
[6] Gurevich A.V., Zybin K.P. and Lukyanov A.V. 1995 *Phys. Rev. Lett.* **75** 2622
[7] Bernhardt P.A. *et al* 2011 *Geophys. Res. Lett.* **38** L19107
[8] Speirs D.C. *et al* 2017 *J. Geophys. Res.* **122** 10–638
[9] Nielsen S.K., Salewski M., Westerhof E., Bongers W., Korsholm S.B., Leipold F., Oosterbeek J.W., Moseev D. and Stejner M. 2013 *Plasma Phys. Control. Fusion* **55** 115003
[10] Hansen S.K., Nielsen S.K., Stober J., Rasmussen J., Stejner M., Hoelzl M. and Jensen T. 2020 *Nucl. Fusion* **60** 106008
[11] Popov A.Y. and Gusakov E.Z. 2015 *Plasma Phys. Control. Fusion* **57** 025022
[12] Klinger T. *et al* 2019 *Nucl. Fusion* **59** 112004
[13] Altukhov A.B., Arkhipenko V.I., Gurchenko A.D., Gusakov E.Z., Popov A.Y., Simonchik L.V. and Usachonak M.S. 2019 *Europhys. Lett.* **126** 15002
[14] Hansen S.K., Jacobsen A.S., Willensdorfer M., Nielsen S.K., Stober J., Höfler K., Maraschek M., Fischer R. and Dunne M. 2021 *Plasma Phys. Control. Fusion* **63** 095002
[15] Gusakov E.Z. and Popov A.Y. 2010 *Phys. Rev. Lett.* **105** 115003
[16] Rapisarda D., Zurro B., Tribaldos V. and Baciero A. (TJ-II Team) 2007 *Plasma Phys. Control. Fusion* **49** 309
[17] Stix T.H. 1992 *Waves in Plasmas* (Berlin: Springer)
[18] Gusakov E.Z. and Popov A.Y. 2021 *Plasma Phys. Control. Fusion* **63** 125017
[19] Gusakov E.Z. and Popov A.Y. 2020 *Plasma Phys. Control. Fusion* **62** 025028
[20] Gusakov E.Z. and Popov A.Y. 2016 *Phys. Plasmas* **23** 082503
[21] Dinklage A. *et al* 2018 *Nat. Phys.* **14** 855–60
[22] Moseev D. *et al* 2019 *Rev. Sci. Instrum.* **90** 013503
[23] Stejner M. *et al* 2014 *Rev. Sci. Instrum.* **85** 093504
[24] Brunner K.J. *et al* 2018 *J. Inst.* **13** P09002
[25] Killer C. *et al* 2019 *Nucl. Fusion* **59** 086013
[26] Zoletnik S. *et al* 2018 *Rev. Sci. Instrum.* **89** 10D107
[27] Omori T. *et al* 2011 *Fusion Eng. Des.* **86** 951–4